Converging cylindrical shocks in ideal magnetohydrodynamics

D. I. Pullin, W. Mostert, V. Wheatley, and R. Samtaney

Articles you may be interested in

Shock dynamics of strong imploding cylindrical and spherical shock waves with real gas effects
Phys. Fluids **22**, 116102 (2010); 10.1063/1.3500684

Generation of cylindrical converging shock waves based on shock dynamics theory
Phys. Fluids **22**, 041701 (2010); 10.1063/1.3392603

Modeling of compressible magnetohydrodynamic turbulence in electrically and heat conducting fluid using large eddy simulation
Phys. Fluids **20**, 085106 (2008); 10.1063/1.2969472

Development of large eddy simulation for modeling of decaying compressible magnetohydrodynamic turbulence
Phys. Fluids **19**, 055106 (2007); 10.1063/1.2728936

Theory of supercompression of vapor bubbles and nanoscale thermonuclear fusion
Phys. Fluids **17**, 107106 (2005); 10.1063/1.2104556

Converging cylindrical shocks in ideal magnetohydrodynamics

D. I. Pullin,[1] W. Mostert,[2] V. Wheatley,[2] and R. Samtaney[3]

[1]*Graduate Aerospace Laboratories, California Institute of Technology, Pasadena, California 91125, USA*

[2]*School of Mechanical and Mining Engineering, University of Queensland, Queensland 4072, Australia*

[3]*Mechanical Engineering, Physical Sciences and Engineering Division, King Abdullah University of Science and Technology, Thuwal, Saudi Arabia*

We consider a cylindrically symmetrical shock converging onto an axis within the framework of ideal, compressible-gas non-dissipative magnetohydrodynamics (MHD). In cylindrical polar co-ordinates we restrict attention to either constant axial magnetic field or to the azimuthal but singular magnetic field produced by a line current on the axis. Under the constraint of zero normal magnetic field and zero tangential fluid speed at the shock, a set of restricted shock-jump conditions are obtained as functions of the shock Mach number, defined as the ratio of the local shock speed to the unique magnetohydrodynamic wave speed ahead of the shock, and also of a parameter measuring the local strength of the magnetic field. For the line current case, two approaches are explored and the results compared in detail. The first is geometrical shock-dynamics where the restricted shock-jump conditions are applied directly to the equation on the characteristic entering the shock from behind. This gives an ordinary-differential equation for the shock Mach number as a function of radius which is integrated numerically to provide profiles of the shock implosion. Also, analytic, asymptotic results are obtained for the shock trajectory at small radius. The second approach is direct numerical solution of the radially symmetric MHD equations using a shock-capturing method. For the axial magnetic field case the shock implosion is of the Guderley power-law type with exponent that is not affected by the presence of a finite magnetic field. For the axial current case, however, the presence of a tangential magnetic field ahead of the shock with strength inversely proportional to radius introduces a length scale $R = \sqrt{\mu_0/p_0}\, I/(2\,\pi)$ where I is the current, μ_0 is the permeability, and p_0 is the pressure ahead of the shock. For shocks initiated at $r \gg R$, shock convergence is first accompanied by shock strengthening as for the strictly gas-dynamic implosion. The diverging magnetic field then slows the shock Mach number growth producing a maximum followed by monotonic reduction towards magnetosonic conditions, even as the shock accelerates toward the axis. A parameter space of initial shock Mach number at a given radius is explored and the implications of the present results for inertial confinement fusion are discussed. © *2014 AIP Publishing LLC*. [http://dx.doi.org/10.1063/1.4894743]

I. INTRODUCTION

The study of shock waves that converge on to either a point or an axis in spherical or cylindrical geometry, respectively, has long been of interest owing to the relevance of shock focusing for inertial confinement fusion.[1,2] Guderley[3] showed that a radially symmetric convergence of strong-shocks in a neutral gas is described by a power-law, Mach-number-radius profile whose exponent could be determined only from consideration of the one-dimensional unsteady Euler equations that govern the shock collapse. Exponents were determined accurately by Butler.[4] A simpler approach to

shock-convergence was introduced by Chisnell[5] who considered the relationship between area and shock strength for a shock moving along a channel.

Whitham[6–8] later generalized this in a two-dimensional unsteady context to the so-called geometrical shock-dynamics, henceforth referred to as GSD, that describes the evolution of shock waves via their interaction with bounding geometry. Geometrical shock dynamics is an inherently nonlinear theory in which shocks propagate down the tubes defined by a system of geometrical rays that are normal to the shock front. The shock motion is determined by information carried on the characteristic of the same family as the shock that enters from behind. For radially symmetric shock convergence, utilization of the shock-jump conditions then gives an ordinary differential equation describing the shock evolution, without the need to determine the post-shock flow field. If the principal interest lies in the shock physics and flow conditions immediately behind the shock, then this reduction of dimensionality is appealing. Geometrical shock dynamics has proved effective for a variety of shock-dynamics problems in multi-dimensional flows including shock focusing in gas dynamics,[9] propagation of shock waves along walls and in channels,[10] shock-wave stability,[7] and shock propagation in non-uniform media.[11] When applied to the symmetrically converging shock of the Guderley type, GSD provides an extremely accurate approximation to power-law exponents and in fact can describe an almost universal shock collapse process from an infinitesimal wave at infinity to a strong-shock state near the point of convergence.[12, 13]

Interest in the effect of a magnetic field on the shock convergence process has been heightened by the knowledge that the presence of a sufficiently strong magnetic field can inhibit the Richtmyer-Meshkov[14, 15] instability that occurs when a shock-wave impacts and impulsively accelerates a perturbed density interface, thereby depositing vorticity and leading to rapid interface growth.[16, 17] Suppression of the Richtmyer-Meshkov instability, while retaining the effects of shock heating, could be expected to have potentially important consequences for the realization of inertial confinement fusion (ICF). Furthermore, it has been experimentally demonstrated that immersing ICF targets in seed magnetic fields results in an increase in observed ion temperature and neutron yield,[18] which is partially attributed to a reduction in heat losses from the center of the implosion due to electron confinement.

A method based on shock dynamics was used by Whitham[19] to conclude that the presence of an axial magnetic field in an ionized gas whose field lines are normal to radially converging particle paths did not affect the power-law convergence of cylindrically converging shocks: see also Gundersen.[20] Presently we revisit this configuration but also consider cylindrical shock convergence in the presence of a singular, azimuthal magnetic field produced by a line current of constant strength coincident with the axis of convergence. The latter will be seen to contain distinct epochs in the radial collapse process and so overall, the flow is not of self-similar form. This case is of particular interest as the use of a similar magnetic field in ICF experiments, generated by a seed current through an axial thin wire, has been suggested as a means to further enhance electron confinement.[18]

In Sec. II we write the equations of motion for non-resistive ideal inviscid magnetohydrodynamics and develop the appropriate characteristic form. A set of restricted shock-jump conditions are then obtained in Sec. III for flow appropriate to cylindrical shocks with a magnetic field orthogonal to particle paths, and zero tangential velocity jump across the shock. The method of GSD is then applied to magnetohydrodynamic shock convergence in Sec. IV. This method is chosen in part owing to its relative simplicity but also because it is not restricted to flow fields with a self-similar structure.[21, 22] It will be seen to be effective for describing the principal physics of symmetrical shock focusing in magnetohydrodynamics, enabling straightforward numerical solution over almost the whole radial domain, while providing some analytical results at small radius. Presently, the case of a bounded axial field is considered first followed by analysis of shock convergence with a singular azimuthal field.

Geometrical shock dynamics is an approximate and not an exact theory. Hence in Sec. V, we apply a finite-volume, shock-capturing method to provide numerical solutions to the full equation set for shock-collapse onto a line current in an ionized gas within the ideal magnetohydrodynamics approximation. Detailed comparisons between the GSD predictions and the full field numerical simulations provide confidence in the present results.

II. EQUATIONS OF MOTION

We consider the non-dissipative and non-resistive magnetohydrodynamic equations in cylindrical co-ordinates (r, θ, z). The flow is assumed to be cylindrically symmetric with the only non-zero velocity component in the radial direction, $u(r, t)$. It is convenient presently to utilize as a variable, the true magnetic field divided by $\sqrt{\mu_0}$, where μ_0 is the permeability of the medium. This is denoted by $\mathbf{B} = (0, B_\theta(r, t), B_z(r, t))$ and will be subsequently referred to as "the magnetic field." The equations of motion can then be written in non-conservative form as

$$\frac{\partial W}{\partial t} + A \frac{\partial W}{\partial r} = -\frac{1}{r} S, \tag{1}$$

where

$$W = \{\rho, u, B_\theta, B_z, p\}^T,$$

$$S = \left\{\rho u, \frac{B_\theta^2}{\rho}, 0, u B_z, a^2 \rho u\right\}^T, \tag{2}$$

$$A = \begin{bmatrix} u & \rho & 0 & 0 & 0 \\ 0 & u & \dfrac{B_\theta}{\rho} & \dfrac{B_z}{\rho} & \dfrac{1}{\rho} \\ 0 & B_\theta & u & 0 & 0 \\ 0 & B_z & 0 & u & 0 \\ 0 & a^2 \rho & 0 & 0 & u \end{bmatrix}, \tag{3}$$

where $\rho(r, t)$ is the fluid density, $p(r, t)$ is the thermodynamic pressure, and $a^2 = \gamma p/\rho$ is the speed of sound.

The eigenvalues of A are $(u, u, u, u \pm c)$, showing that, for the present restricted one-dimensional flow with $u_t = B_n = 0$, the slow and intermediate speeds collapse to zero while the fast speed collapses to the fast magnetosonic wave speed

$$c = \sqrt{a^2 + \frac{B_\theta^2 + B_z^2}{\rho}}. \tag{4}$$

Our interest is in the characteristic equation corresponding to the wavespeed $u - c$, which is the characteristic entering the shock from behind. The left eigenvector for this case is

$$\left\{0, 1, -\frac{B_\theta}{\rho c}, -\frac{B_z}{\rho c}, -\frac{1}{\rho c}\right\}, \tag{5}$$

and the corresponding characteristic equation is given by

$$\frac{du}{dt} - \frac{1}{\rho c} \frac{d}{dt}\left(p + \frac{1}{2}(B_\theta^2 + B_z^2)\right) = -\frac{1}{r}\left[\frac{B_\theta^2}{\rho} - u\left(\frac{a^2}{c} + \frac{B_z^2}{\rho c}\right)\right], \tag{6}$$

on $dr/dt = u - c$. Using the chain rule for the time derivative, this can be written as

$$-\rho c \frac{du}{dr} + \frac{d}{dr}\left(p + \frac{1}{2}(B_\theta^2 + B_z^2)\right) = \frac{1}{r}\frac{\rho c}{u - c}\left[\frac{B_\theta^2}{\rho} - u\left(\frac{a^2}{c} + \frac{B_z^2}{\rho c}\right)\right]. \tag{7}$$

The above equations govern the evolution of a quasi-neutral conducting fluid when resistive and viscous effects are negligible, which requires the magnetic and hydrodynamic Reynolds numbers to be large. The ideal MHD approximation also requires that the plasma must be highly collisional, so it can be treated as a continuum, and that the ion Larmor radius be small compared to the characteristic length scales of the flow. To assess whether these conditions may be violated in the present flows requires knowledge of the solutions. These will be discussed later.

III. MHD SHOCK JUMP CONDITIONS

In the frame of reference in which the shock is stationary, the explicit MHD shock jump conditions are

$$\left[\rho\, u'_n \right] = 0, \tag{8}$$

$$\left[\rho\, u'^2_n + p + \frac{1}{2}\, B_t^2 \right] = 0, \tag{9}$$

$$\left[\rho\, u'_n u'_t - B_n\, B_t \right] = 0, \tag{10}$$

$$\left[\frac{\rho\, u'_n}{2} \left(u'^2_n + u'^2_t \right) + \frac{\gamma\, u'_n\, p}{\gamma - 1} + u'_n\, B_t^2 - u'_t\, u'_t\, B_t \right] = 0, \tag{11}$$

$$\left[u'_n\, B_t - u'_t\, B_n \right] = 0, \tag{12}$$

where B_n and B_t are the reduced magnetic fields normal and tangential to the shock, respectively, u'_n and u'_t are the fluid speeds normal and tangential to the shock, respectively, in shock-fixed co-ordinates, γ is the ratio of specific heats, and $[Q]$ represents the jump of Q across the shock. In the present application we will consider a cylindrical shock imploding onto the axis at $r = 0$. Conditions upstream of shock in the laboratory frame of reference will then be taken as $u = 0$, $\rho_0 = $ constant, $p_0 = $ constant, and magnetic field $B_0(r)$, which is tangential to the shock and could be either B_θ, B_z or some combination of these. In this configuration we will set $B_n = 0$, $u_t = u'_t = 0$. For the normal velocity the transformation from shock-fixed to laboratory co-ordinates is $u = u'_n - U_S$ where u is radial velocity, and $U_s > 0$ is the shock speed. The tangential magnetic field B_t will again be either B_θ or B_z. The shock jump conditions obtained below under these conditions will be referred to as the *restricted jump conditions*.

From (4) the MHD wave speed ahead of the shock can be written as

$$c_0(r)^2 = a_0^2 + \frac{B_0^2(r)}{\rho_0}, \quad a_0^2 = \gamma\, \frac{p_0}{\rho_0}. \tag{13}$$

The local shock Mach number and the ratio of the sound speed ahead of the shock to the single MHD speed ahead of the shock are defined, respectively, by

$$M \equiv \frac{U_s}{c_0}, \quad \epsilon \equiv \frac{a_0^2}{c_0^2}. \tag{14}$$

Since by (13), a strong magnetic field gives $c_0 \gg a_0$, then this case will correspond to $\epsilon \ll 1$. It will later be seen that presently, $U = U(r, t)$, $\epsilon = \epsilon(r)$.

With these definitions the local, restricted shock-jump conditions for density and pressure can be determined from (8) to (12) as

$$\eta \equiv \frac{\rho}{\rho_0} = \frac{-\epsilon(2 - \gamma) - (\gamma - 1)M^2 - \gamma + G(\epsilon, M^2, \gamma)}{2(1 - \epsilon)(2 - \gamma)}, \tag{15}$$

$$G(\epsilon, M^2, \gamma) = \sqrt{4(1 - \epsilon)(2 - \gamma)(\gamma + 1)M^2 + \left(\epsilon(2 - \gamma) + (\gamma - 1)M^2 + \gamma \right)^2}, \tag{16}$$

$$\frac{p}{p_0} = 1 + \frac{1}{2} \left(\frac{1}{\epsilon} - 1 \right) \left(1 - \eta^2 \right) \gamma + \frac{\left(1 - \frac{1}{\eta} \right) \gamma M^2}{\epsilon}. \tag{17}$$

From (15) it can be shown that $\eta \geq 1$ requires that $(\epsilon - 1)(2 - \gamma)(M^2 - 1) \leq 0$. Since $0 < \epsilon \leq 1$, this is satisfied with $2 > \gamma$, $M^2 > 1$. In a frame of reference in which the upstream gas is

stationary (laboratory frame), the gas speed and magnetic field immediately behind the shock can be obtained as

$$u = -M c_0 \left(1 - \frac{1}{\eta}\right), \quad B_t = B_0 \, \eta, \tag{18}$$

and we note that for the converging shock, $u < 0$. The sound speed and the MHD speed behind the shock can be calculated from the other jump conditions using

$$a^2 = \gamma \, \frac{p}{\rho}, \quad c^2 = a^2 + \frac{B_t^2}{\rho}. \tag{19}$$

If $B_0 = 0$ then $\epsilon = 1$ and it can be shown that the restricted shock-jump conditions reduce to the standard gas-dynamic jump conditions. We remark that care must be taken in this limit owing to the singular denominator in the expression for the jump in density.

The form of the shock jump conditions for $M - 1 \ll 1$ are

$$\frac{\rho}{\rho_0} = 1 + \frac{4}{3 - \epsilon \, (2 - \gamma)} \, (M - 1) + O\left((M - 1)^2\right), \tag{20}$$

$$\frac{p}{p_0} = 1 + \frac{4 \, \gamma}{3} \, (M - 1) + \frac{2 \, \gamma \, (8 \, \gamma - 7)}{27} \, (M - 1)^2$$
$$+ \frac{16 \, \gamma \, (\gamma - 1)}{27} \, \frac{(M - 1)^3}{\epsilon} + O\left(\frac{(M - 1)^4}{\epsilon}\right). \tag{21}$$

For $M \gg 1$ we find that

$$\frac{\rho}{\rho_0} = \frac{\gamma + 1}{\gamma - 1} - \frac{2 \, (\gamma + 1)}{(\gamma - 1)^3} \, \frac{1}{M^2} + O\left(\frac{\epsilon}{M^2}\right), \tag{22}$$

$$\frac{p}{p_0} = \frac{1}{\epsilon} \left(\frac{2 \, \gamma}{\gamma + 1} \, M^2 - \frac{2 \, (\gamma^2 + 2 \, \gamma - 1)}{(\gamma + 1) \, (\gamma - 1)^2}\right) + O\left(\frac{1}{M^2}\right). \tag{23}$$

We define a strong shock as $p/p_0 \gg 1$. This is obtained with either $M \gg 1$ with $\epsilon = O(1)$ or by $\epsilon \ll 1$ with $M - 1 = O(1)$. That is, strong shock conditions can be achieved by either large Mach number or by a strong magnetic field. The fourth term on the right-side of Eq. (21) contains a potential distinguished limit $(M - 1)^3/\epsilon$ when both $M \to 1$ and $\epsilon \to 0$.

IV. GEOMETRICAL SHOCK DYNAMICS

An ordinary differential equation for the variation of the shock Mach number with (r, t) can be obtained by applying Whitham's[8] GSD to the present system. We can derive the equations of GSD by a linearization of the full equations in the region behind the collapsing shock. A far simpler method is provided by the direct application to the present equation set of Whitham's characteristic rule. This states that

Write down the exact nonlinear differential relation for the C+ characteristics. Substitute the expressions for p, ρ, u, a in terms of M from the shock jump conditions. The resulting differential equation gives the variation of M with r.

This can be applied directly to Eq. (7), with all required shock conditions given explicitly by Eqs. (15) and (17)–(19). In general the shock converges into a non-uniform medium in the sense that $c_0 = c_0(r)$ and $\epsilon = \epsilon(r)$. This means that all shock jump conditions are functions of both M and r. The ordinary differential equation for $M(r, t)$ is then

$$\frac{dM}{dr} = \frac{\dfrac{1}{r} \dfrac{\rho \, c}{(u - c)} \left[\dfrac{B_\theta^2}{\rho} - u \left(\dfrac{a^2}{c} + \dfrac{B_z^2}{\rho \, c}\right)\right] - \left(\dfrac{\partial p^*}{\partial r} - \rho \, c \, \dfrac{\partial u}{\partial r}\right)}{\dfrac{\partial p^*}{\partial M} - \rho \, c \, \dfrac{\partial u}{\partial M}}, \tag{24}$$

$$p_* = p + \frac{1}{2}\left(B_\theta^2 + B_z^2\right), \tag{25}$$

where p_* is the magnetic pressure and it is understood that all quantities on the right-hand side are evaluated from the shock-jump conditions.

A. Gas-dynamics case

When $B_z = B_\theta = 0$, then $c = a$, $\epsilon = 1$ and the shock jump conditions for density and pressure are

$$\frac{\rho}{\rho_0} = \frac{(\gamma + 1)M^2}{2 + (\gamma - 1)M^2}, \tag{26}$$

$$\frac{p}{p_0} = \frac{2\gamma M^2 - (\gamma - 1)}{\gamma + 1}, \tag{27}$$

together with jump conditions for u, c that depend only on γ and M. Then (24) and (25) reduce to the strictly gas dynamics case[8]

$$\frac{dM}{dr} = -\frac{1}{r}\frac{M^2 - 1}{M\,\lambda(M)}, \tag{28}$$

$$\lambda(M) = \left(1 + \frac{2}{\gamma + 1}\frac{1 - \mu^2}{\mu}\right)\left(1 + 2\mu + \frac{1}{M}\right), \tag{29}$$

$$\mu^2 = \frac{(\gamma - 1)M^2 + 2}{2\gamma M^2 - (\gamma - 1)}. \tag{30}$$

Whitham gives an integral expression of the form $r = r(M)$ for the general case for both cylindrical and spherical convergence. For the cylindrical strong shock limit $M \gg 1$, $\lambda(M) \to n$, where

$$n = 1 + \frac{2}{\gamma} + \sqrt{\frac{2\gamma}{\gamma - 1}}, \tag{31}$$

and then (28) may be integrated to give

$$M = M_0\left(\frac{r}{r_0}\right)^{-\frac{1}{n}}. \tag{32}$$

For $\gamma = 5/3$, $1/n = 0.225425$ compared to the exact Guderley solution where the exponent in (32) is 0.226054.[4] The weak shock limit can be obtained when $M - 1 \ll 1$. In this case $\lambda(M) \to 1$ and, with $m = M - 1$, the right-side of (28) is $-m/(2\,r)$ plus higher order terms. This gives the weak-shock result

$$M - 1 \sim \left(\frac{r}{r_0}\right)^{-\frac{1}{2}}. \tag{33}$$

Hence a converging cylindrical, initially weak shock will always evolve towards the strong-shock limit.

For non-zero magnetic field, when $\epsilon < 1$, the right-hand side of (24) can be evaluated as an algebraic function of M, ϵ but the result is extremely cumbersome and so will not be given explicitly. Equation (24) can however be accurately solved numerically for a given set of parameters, and this will be done presently. Asymptotic results can also be obtained when $r \ll 1$.

B. Presence of a magnetic field

In what follows we consider a cylindrical shock initialized at $r = r_0$ with Mach number M_0. We will presently consider two separate cases described below.

1. Constant axial magnetic field

Here the magnetic field is uniform ahead of the shock,

$$B_\theta \equiv 0, \quad B_0 \equiv B_z = \text{constant}, \tag{34}$$

where B_0 is constant. We non-dimensionalize B_0 by $\sqrt{p_0}$ and characterize the magnetic field strength by the parameter

$$\beta \equiv \frac{2 p_0}{B_0^2}, \tag{35}$$

which is constant. Also, pressure, density, and velocity are non-dimensionalized, respectively, by p_0, ρ_0, and $\sqrt{p_0/\rho_0}$. The constant MHD wave speed and ϵ are then

$$c_0^2 = \gamma + \frac{2}{\beta}, \quad \epsilon = \frac{\beta \gamma}{\beta \gamma + 2}. \tag{36}$$

In anticipation of a strong shock for small r, we consider the strong shock $M \gg 1$. For a uniform magnetic field ahead of the shock ϵ is constant and so the explicit r-derivatives in (24) vanish. The only r-dependence on the right-hand side is then the r^{-1} pre-factor. Upon substituting the $M \gg 1$ forms of the shock jump conditions into the right-hand side of (24) and obtaining the large M limit, the shock-dynamic ordinary-differential equation (ODE) takes the form

$$\frac{dM}{dr} = -\frac{1}{n} \frac{M}{r} + \frac{1}{r} \frac{f(\beta, \gamma)}{M} + \dots, \tag{37}$$

where n is given by (31) and

$$f(\beta, \gamma) = \frac{\sqrt{\gamma}(\gamma + 1) q(\beta, \gamma)}{4 \left(\gamma^2 + \sqrt{2(\gamma - 1)\gamma} + \gamma - 2\right)^2 (\beta\gamma + 2)}, \tag{38}$$

$$q(\beta, \gamma) = (8\beta - 4)\gamma^{7/2} - 4(5\beta - 3)\gamma^{5/2} + 4(4\beta + 5)\gamma^{3/2} + \sqrt{2}(5\beta - 2)\sqrt{\gamma - 1}\gamma^3 \tag{39}$$
$$+ \sqrt{2}(6 - 7\beta)\sqrt{\gamma - 1}\gamma^2 - 4(\beta + 3)\sqrt{\gamma} + 20\sqrt{2}\sqrt{\gamma - 1}\gamma - 4\sqrt{2}\sqrt{\gamma - 1}.$$

To leading order this gives

$$M = M_0 \left(\frac{r}{r_0}\right)^{-\frac{1}{n}} + O(r^{\frac{1}{n}}). \tag{40}$$

In the above, the function $f(\beta, \gamma)$ is bounded for all finite β and $\gamma > 1$. It can be noted that Eq. (40) agrees with (32) for the gas dynamics case. Hence, to leading order shock-dynamics predicts that the presence of a uniform, transverse magnetic field does not affect the power-law strengthening of the shock in convergence onto the axis, in agreement with Refs. 19 and 20. Numerical solutions of the full shock-dynamics ODE, not shown presently, confirm this result. It is expected that this result will be valid for any axial field that is a function of r only and is bounded when $r \to 0$.

2. Shock collapse onto a line current

A magnetic field ahead of the shock is generated by a line current I of infinite extent along the axis $r = 0$. The true and reduced magnetic fields are azimuthal and can then be written as

$$\hat{B}_\theta(r) = \frac{\mu_0 I}{2 \pi r}, \quad B_0 \equiv B_\theta(r) = \frac{\sqrt{\mu_0} I}{2 \pi r}. \tag{41}$$

A length scale or critical radius can be defined as $R = \sqrt{\mu_0/p_0} I/(2 \pi)$. We normalize $\hat{B}$ by $\sqrt{p_0 \mu_0}$, ρ and p by ρ_0, p_0, respectively, r by R and keep the same symbols, (B_θ, r), for non-dimensional quantities. The dimensionless magnetic field ahead of the shock is then

$$B_0(r) \equiv B_\theta(r) = \frac{1}{r}, \quad B_z = 0. \tag{42}$$

Hence for $r > R$ the field strength is weak but is strong for $r < R$. Further

$$c_0(r)^2 = \gamma + \frac{1}{r^2}, \quad \epsilon = \frac{\gamma}{\gamma + \frac{1}{r^2}}, \quad \epsilon = \gamma \, r^2 + \mathcal{O}(r^4), \quad r \ll 1. \tag{43}$$

The right-hand side of (24) contains variables ρ, a, c, B_θ, p, ... together with the derivatives of both $p*$ and u with respect to r and M. The shock jump conditions provide values of the same variables immediately behind the shock as functions of M, γ and also of r because $\epsilon = \epsilon(r)$ given by the second equation in (43). To obtain the GSD ODE in an explicit form, the derivatives $\partial p*/\partial M$, $\partial u/\partial M$, $\partial p*/\partial r$, $\partial p*/\partial r$ are first obtained by differentiation of the relevant shock-jump conditions. These quantities and the shock jump conditions themselves are then substituted directly into (24). Since all quantities are now functions of M, γ, r, (24) is of the form

$$\frac{dM}{dr} = -\frac{1}{r} \, F(M, \gamma, r), \tag{44}$$

where the $F(M, \gamma, r)$ is a known function of its arguments. All algebraic constructions are done symbolically using Mathematica-9 and so the final form of (44), which is not suitable for explicit reproduction presently, exists only within a Mathematica script. Nonetheless this allows both asymptotic analysis and numerical solution.

Putting $M = 1 + m$, we explore the limit $m \ll 1$ for r small. This can be done either using the full symbolic form of (44), or, as was done presently by substituting (20)–(22) together with corresponding approximations for the $m \ll 1$ forms of other shock jump conditions into the right-hand side of (24) and expanding the resultant approximate form of $F(M, \gamma, r)$ in (44) as a Taylor series for $m \ll 1$, $r \ll 1$, ensuring that the result does not depend on the order of the expansion. This was done with Mathematica and the leading-order checked manually, with the result that the form of the shock-dynamics ODE becomes

$$\frac{dm}{dr} = \frac{m}{r} \left[1 + m \frac{4\gamma - 11}{18} + \mathcal{O}(m^2) \right]$$
$$+ m \, r \left[\frac{\gamma \, (4\gamma - 17)}{6} + m \frac{\gamma \, (40 \, \gamma^2 - 316 \, \gamma + 535)}{108} + \mathcal{O}(m^2) \right] + \mathcal{O}(m^2 \, r^2). \tag{45}$$

This suggests the asymptotic form, for $m \ll 1$

$$\frac{dm}{dr} = \frac{m}{r} \left[1 + \sum_{n=1}^{\infty} a_n(\gamma) \, m^n \right] + \sum_{k=1}^{\infty} \sum_{n=0}^{\infty} b_{kn}(\gamma) r^k \, m^{k+n}. \tag{46}$$

There is a regular singular point at $r = 0$ whose coefficient is independent of γ. Assuming that the series in (46) converges to a function of r, m that is analytic near $r = 0$, $m = 0$, this gives the leading-order solution for small r

$$M = 1 + A \, r + \mathcal{O}(r^2), \tag{47}$$

where A is independent of γ and will generally depend on initial conditions. This result indicates that any cylindrically converging shock, as it approaches the origin, weakens to approach a magnetosonic wave. When $r \to 0$, the wave speed diverges as $1/r$.

Although the right-hand-side of (44) is unwieldy it is nonetheless straightforward to integrate this equation numerically as a nonlinear, first-order ODE, for given γ and $M(r = r_0) = M_0$. In fact while the shock trajectory has physical meaning only as a time-wise convergence towards the origin, the GSD ODE can be reversibly integrated for either r decreasing or increasing from some initial condition. All numerical integrations of (44) described presently were performed for $\gamma = 5/3$ using the *NDSolve* command within Mathematica-9 for the numerical solution of ordinary differential equations. Each numerical solution uses dynamically variable stepsize with a solution provided as an interpolating polynomial over the range of r chosen. Several options including a desired accuracy parameter were utilized to obtain confidence in the accuracy of solutions to six significant figures. For given γ, all possible solutions to (44) conform to a one-parameter family for which a unique

TABLE I. Eight shock-dynamics cases. Mach numbers at three radii: $r = 10^6, r = 10^4; r = 1$. T_c is shock collapse time from $r = 10^6$.

$r = 10^6$	$r = 10^4$	$r = 1$	T_c
35.42	100.0	630.41	1.7846×10^4
10.66	30.0	189.04	5.9357×10^4
3.65	10.0	62.76	1.7466×10^5
1.69	4.0	24.50	3.9393×10^5
1.16	2.0	11.06	6.1410×10^5
1.0109	1.1	2.23	7.5897×10^5
1.0010	1.01	1.448	7.7306×10^5
1.0000984	1.001	1.0682	7.7444×10^5

solution is defined by an arbitrary $M = M_0 > 1$ at a defined reference radius r_0. In the examples shown presently we choose $r_0 = 10^4$ and eight cases with $M_0 = 100.0, 30.0, 10.0, 4.0, 2.0, 1.1, 1.01, 1.001$. For each of these initial conditions (44) was solved numerically as described over two ranges; inward over $10^{-6} \leq r \leq 10^4$ and also outward with $10^4 \leq r \leq 10^6$. When joined at $r = 10^4$, these provide composite solutions over 12 decades in radius.

For the eight cases Table I shows M at each of three radii $r = 10^6, r = 10^4, r = 1$. Figure 1(a) shows $M(r)$ while Figure 1(b) gives $M - 1$ versus r, both as log-log plots. Starting from $r = 10^6$ it can be seen that, for all cases, $M(r)$ increases to a maximum near $r = 1$ and then decreases toward the origin. Three distinct regimes are visible in Figure 1(b). When $r \gg 1$ and $M - 1 \ll 1$, the magnetic field is weak and the shock convergence behaves like the gas-dynamic weak-shock case with $M - 1 \sim r^{-1/2}$. But if $r \gg 1$ and $M \gg 1$ this is clear evidence of gas-dynamic strong-shock behavior with $M \sim r^{-0.2245}$. When $r \to 0$, weak-shock linear behavior $M - 1 \sim r$ in agreement with (47) is seen for all cases.

The variation of the shock radius $R_s(t)$ for $t < 0$ is displayed in Figure 2 where the origin of time is such that $R_s \to 0$ when $t \to 0$ from below. These were obtained by numerically integrating the ODE $dR_s(t)/dt = M(r) c_0(r)$ where $M(r)$ is obtained from the shock-dynamics and $c_0(r) = \sqrt{\gamma + r^{-2}}$. In Figure 2 the initial shock strength at r_0 decreases upward. The uppermost curve is a limit given by
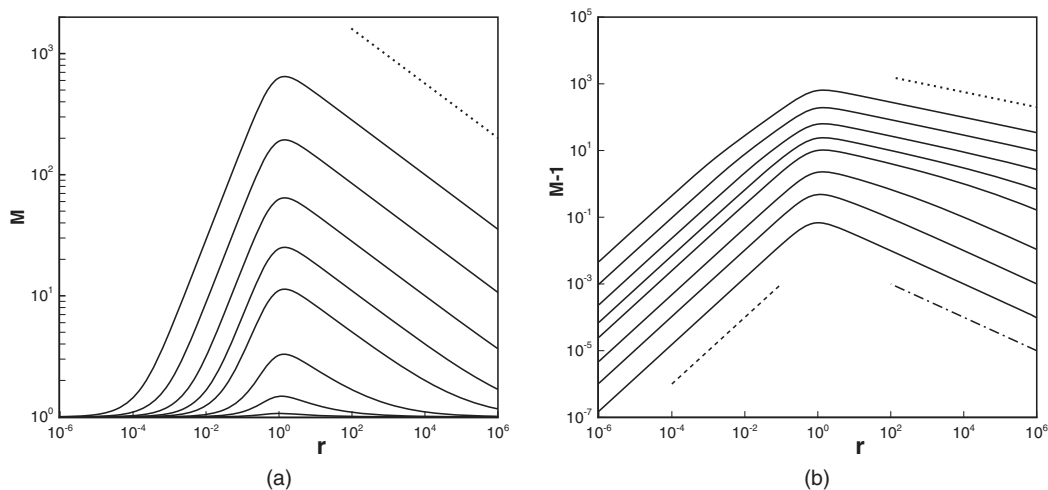

FIG. 1. Mach number versus radius obtained from shock dynamics (GSD). (a) M(r), (b) M(r)−1. Solid lines: GSD results obtained by specifying a given Mach number at $r = r_0$. From top to bottom: M_0 at $r_0 = 10^4$ with $M_0 = 100, 10, 4, 2, 1.1, 1.01, 1.001$. Dashed line: $M - 1 \sim r$; dotted-dashed, gas-dynamic weak shock $M - 1 \sim r^{-1/2}$; dotted, gas dynamic strong shock $M \sim r^{-0.2254}$ for $\gamma = 5/3$.
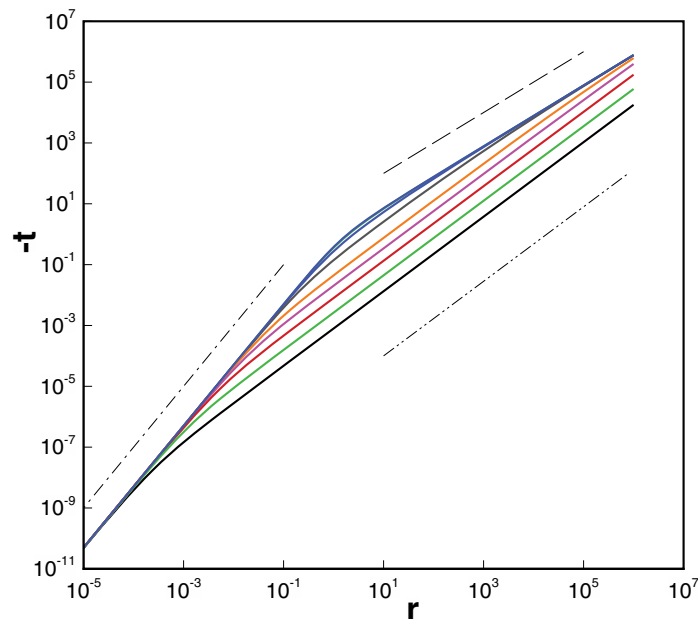
FIG. 2. Shock radius versus $-t$, log-log. Solid lines: SD results obtained by specifying a given Mach number at $r = r_0$. From bottom to top: M_0 at $r_0 = 10^4$ with $M_0 = 100, 10, 4, 2, 1.1, 1.01, 1.001, 1+$. The $M_0 = 1+$ case is the trajectory of a magnetosonic wave. Dashed line: $R_s \sim -t$; dotted-dashed, $R_s \sim (-t)^{1/2}$; dotted-dotted-dashed, gas-dynamic strong shock $R_s \sim (-t)^{0.8161}$ for $\gamma = 5/3$.

the passage of a cylindrical magnetosonic wave defined by the ODE $dR_s(t)/dt = c_0(r)$ with solution

$$R_s(t) = \left[\frac{((1 - \gamma\, t)^2 - 1)}{\gamma} \right]^{1/2}, \quad t \le 0. \tag{48}$$

In Figure 2 all shock trajectories become asymptotic to the magnetosonic wave solution $r = \sqrt{-2t} + O((-t)^{3/2})$, $t \to 0$. Also shown are the slope of the large $-t$ magnetosonic asymptote $r = -\sqrt{\gamma}\, t + O(1)$, $t \to -\infty$ and the gas-dynamic strong-shock approximation $r \sim (-t)^{0.8161}$.

Figure 3(a) shows $p(r)$ with $p(r) - 1$ shown in Figure 3(b) while Figure 4(a) shows the variation of the density ratio $\rho/\rho_0(r)$. It can be seen that the maximum in the pressure ratio moves progressively towards the origin as $M(r_0 = 10^4)$ increases, and, generally, does not coincide with the Mach-number maximum. For shocks for which $M(r = 1) \gg 1$, the density ratio achieves its maximum $\rho/\rho_0|_{max} = (\gamma + 1)/(\gamma - 1)$ (which is 4 for $\gamma = 5/3$), a value which is not affected by the presence of the magnetic field. But as the shock eventually weakens when $r \to 0$, a roll-off in the density ratio occurs at about the same position as the pressure maximum. The behavior of the pressure can be attributed to the fourth term, of order $(M - 1)^3/\epsilon$ on the right-side of the $M - 1 \ll 1$ pressure-jump expression, (22). It can be seen from (22) that with $M - 1 \sim r$ given by (47), and with, $\epsilon \sim r^2$, $r \ll 1$, then $(M - 1)^3/\epsilon \sim O(r)$ when $r \ll 1$. Therefore, the pressure jump becomes small when $r \to 0$. Hence, while $(M - 1)^3/\epsilon \ll 1$ will eventually be reached for all cases, this occurs at smaller radius for initially stronger shocks, an effect that can be clearly seen in Figure 4(b). In particular, for our strongest shock case, $p(r = 10^{-6})/p_0 \sim O(10^4)$ while from Figure 1(b), $M(r = 10^{-6}) - 1 \sim O(10^{-2})$.

V. NUMERICAL SOLUTION OF ONE-DIMENSIONAL MHD EQUATIONS

A. Numerical method

In this section we describe the method used to obtain the numerical solutions to the ideal MHD equations presented in this work. The scheme is based essentially on minor modifications of the method described in detail in Samtaney *et al.*[23] The original code is an unsplit adaptive mesh conservative code for the resistive MHD equations. For the purposes of the 1D numerical simulations presented in this paper, we switched off the "transverse predictor" of the unsplit method. Moreover,
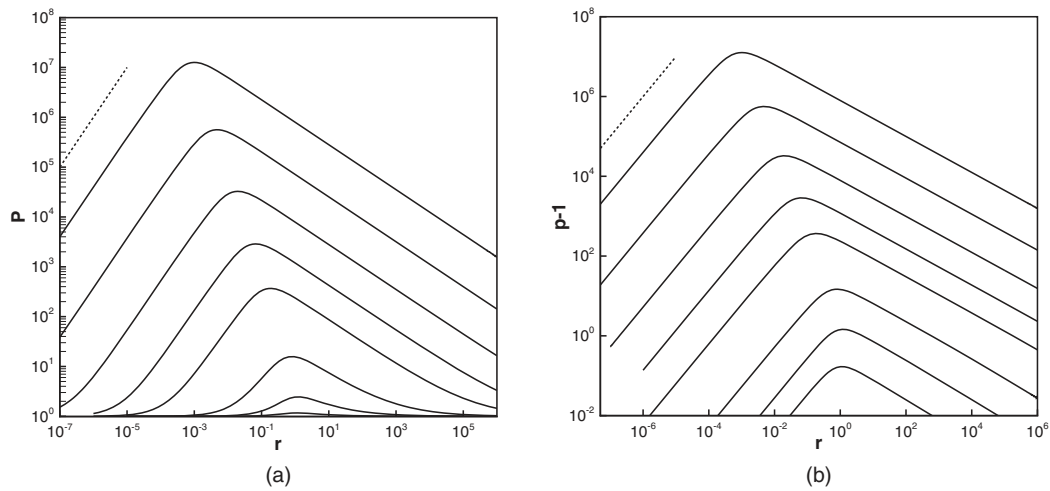
FIG. 3. Pressure ratio across shock from shock dynamics (GSD). (a) $p(r)$ and (b) $p(r) - 1$. Solid line: GSD results. For key, see Figure 1.

the diffusion terms are switched off. The other modifications include stretching the mesh in the radial direction with an analytical stretching (exponential) function, and subtracting a curl-free part of the magnetic field (see discussion below) in an approach similar to that described in Powell *et al.*[24] The MHD code utilized in this paper utilizes essentially the same code base, and the same routines for the Riemann solver, slope limiting, etc., as the one in Samtaney *et al.*, which has been amply tested and verified. The verifications tests include: linear wave propagation tests, regular shock refraction at a density interface in MHD (this example is truly a multidimensional verification of the solution in the neighborhood of shock refraction and described in thorough detail in Wheatley *et al.*[25]), and magnetic reconnection.[23] Furthermore, convergence tests in a variety of contexts have been presented in Wheatley *et al.*[17,26] For completeness, we present the equations and numerical method below.

For the purposes of numerical solution, it is convenient to write the one-dimensional equations in conservation form as follows:

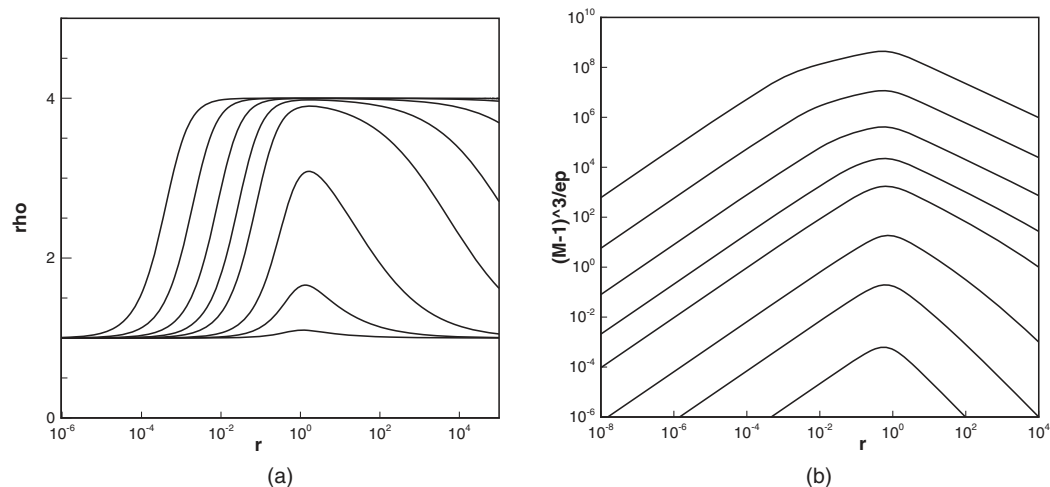$$\frac{\partial U}{\partial t} + \frac{1}{r}\frac{\partial (r F)}{\partial r} = S, \tag{49}$$

FIG. 4. (a) Density ratio across shock. (b) $(M - 1)^3/\epsilon(r, \gamma)$, $\gamma = 5/3$. For key, see Figure 1.

where $U = \{\rho, \rho u, B_\theta, B_z, e\}^T$, where e is the total energy per unit volume. Note that here we are using the energy equation in place of the entropy equation used in (1), which is equivalent for inviscid, non-dissipative MHD. The flux $F(U)$ and source $S(U)$ are given by

$$F(U) = \{\rho u, \rho u^2 + p_t, B_\theta u, B_z u, (e + p_t)u\}^T,$$

$$S(U) = \frac{1}{r}\{0, p_t - B_\theta^2, B_\theta u, 0, 0\}^T, \tag{50}$$

where the magnetic pressure p_t is given by (25). The total energy e is related to the pressure as follows:

$$e = \frac{p}{\gamma - 1} + \frac{1}{2}\rho u^2 + \frac{1}{2}(B_\theta^2 + B_z^2). \tag{51}$$

Rewriting the azimuthal component of the magnetic field as $B_\theta = B_\theta^0 + B_\theta^1$, with $B_\theta^0 = \frac{1}{r}$, allows us to cancel terms proportional to r^{-3} in the radial momentum equation. Without this analytical cancellation, large numerical errors occur close to the origin. The above equations are then rewritten as

$$\frac{\partial \tilde{U}}{\partial t} + \frac{\xi'(r)}{r}\frac{\partial(r\tilde{F})}{\partial \xi} = \tilde{S}, \tag{52}$$

where the solution vector is modified as $\tilde{U} = \{\rho, \rho u_r, B_\theta^1, B_z, \tilde{e}\}^T$. In order to resolve flow features more accurately near the origin, we employ an analytical mesh stretching function denoted by $\xi \equiv \xi(r)$. For the results presented in this paper, this stretching function is chosen to be exponential to provide a much smaller mesh spacing near the origin. The modified flux and source terms are

$$\tilde{F}(U) = \{\rho u, \rho u^2 + \tilde{p}_t + B_\theta^0 B_\theta^1, B_\theta u, B_z u$$
$$(\tilde{e} + \tilde{p} + B_\theta^0 B_\theta^1)u\}^T,$$

$$\tilde{S}(U) = \frac{1}{r}\{0, \tilde{p}_t - (B_\theta^0 + B_\theta^1)B_\theta^1, 0, B_\theta u, 0, 0\}^T, \tag{53}$$

where $\tilde{p}_t = p + \frac{1}{2}((B_\theta^1)^2 + B_z^2)$ and $\tilde{e} = \frac{p}{\gamma - 1} + \frac{1}{2}\rho u^2 + \frac{1}{2}((B_\theta^1)^2 + B_z^2)$.

Equation (52) is solved using a finite volume upwind method as described below. The radial domain is discretized into finite volumes and each finite volume is index by i with faces at $i \pm \frac{1}{2}$. The numerical method is a predictor-corrector method wherein we first predict the solution at time $n + \frac{1}{2}$ at the finite volume faces. To achieve this, we first define a vector of primitive variables $W \equiv W(U) = \{\rho, u, B_\theta, B_z, p\}^T$. Rewriting the equations using W in quasilinear form, we get

$$\frac{\partial W}{\partial t} + A\xi'(r)\frac{\partial W}{\partial \xi} = S_p, \tag{54}$$

which is the same form as in (52).

A Taylor series yields the predicted primitive variables at the finite volume faces as follows:

$$\begin{aligned}
W_{i\pm\frac{1}{2},S}^{n+\frac{1}{2}} &= W_i^n + \frac{1}{2}\Delta t\left(\frac{\partial W}{\partial t}\right)_i^n \pm \frac{1}{2}\Delta\xi\left(\frac{\partial W}{\partial \xi}\right)_i^n \\
&= W_i^n - \frac{1}{2}\Delta t\left[A_i^n\xi'(r_i)\left(\frac{\partial W}{\partial \xi}\right)_i^n + S_{p,i}^n\right] \pm \frac{1}{2}\Delta\xi\left(\frac{\partial W}{\partial \xi}\right)_i^n \\
&= W_i^n + \frac{1}{2}\Delta t S_{p,i}^n - \frac{1}{2}\left(\pm I - A_i^n\xi'(r_i)\frac{\Delta t}{\Delta\xi}\right)\Delta W_i^n,
\end{aligned} \tag{55}$$

where $(\pm, S)$ is either $(+, L)$ or $(-, R)$ with L (resp. R) indicating the left (resp. right) predicted state at the cell interface. We fit linear profiles in each computational cell, and compute undivided slopes ΔW which are subsequently limited in characteristic space using Van Leer slope limiting. This is

achieved by replacing the final step above as follows:

$$W_{i\pm\frac{1}{2},S}^{n+\frac{1}{2}} = W_i^n + \frac{1}{2}\Delta t\, S_{p,i}^n - \frac{1}{2}\left(\pm I - A_i^n \xi'(r_i)\frac{\Delta t}{\Delta\xi}\right)\mathcal{P}_\pm(\Delta W_i^n),\tag{56}$$

where $\mathcal{P}_\pm(W) = \sum_{\pm\lambda_k>0}(l_k \cdot W)r_k$, where λ_k are eigenvalues of A, and l_k and r_k are the corresponding left and right eigenvectors. The left and right predicted states at every cell interface above constitute a Riemann problem. A standard linearized solver is used to obtain the solution, denoted as W^{RP} of the Riemann problem as

$$\tilde{W}^{RP} = W_L + \sum_{\lambda_k>0}[l_k \cdot (W_R - W_L)]r_k$$

$$= W_R - \sum_{\lambda_k<0}[l_k \cdot (W_R - W_L)]r_k,\tag{57}$$

where λ_k, l_k, and r_k are computed at the arithmetic average of W_L and W_R.

This is then used to compute the numerical fluxes and the solution updated in each finite volume as

$$\tilde{U}_i^{n+1} = \tilde{U}_i^n - \frac{\Delta t\,\xi'(r_i)}{r_i\,\Delta\xi}\left(r_{i+\frac{1}{2}}\tilde{F}_{i+\frac{1}{2}}^{n+\frac{1}{2}} - r_{i-\frac{1}{2}}\tilde{F}_{i-\frac{1}{2}}^{n+\frac{1}{2}}\right) + \Delta t\,S_i^n,\tag{58}$$

where $\tilde{F}_{i\pm\frac{1}{2}}^{n+\frac{1}{2}} \equiv \tilde{F}(W_{i\pm\frac{1}{2}}^{RP})$. The code has an optional explicit second-derivative artificial viscosity term proportional to $\Delta\xi^2$ to filter grid level oscillations should these occur.

B. Comparison of numerical solution with shock dynamics

Numerical simulations of the one-dimensional equations reported presently were performed using an exponentially stretched grid with $N = 16 \times 10^3$ grid points and $\gamma = 5/3$. A resolution study of the convergence of solutions for shock properties is discussed below. The initial condition was a shock initiated at $r = r_0$ with given M_0. Conditions ahead of the shock were quiescent with post-shock conditions, calculated using the restricted shock jump conditions, painted uniformly in a few cells behind the initial shock position. This generally resulted in a start-up transient but this was always small. Four cases with initial conditions using $M_0 = 100, 10, 2, 1.1$ at $r_0 = 10^2$ were explored. These are different to the previously described cases with M_0 given at $r = 10^4$ because, even with a large number of radial points, the numerical solutions of the full MHD equations cannot cover the full radial domain used in the shock-dynamics calculations. For all the present cases, independent shock-dynamics solutions were obtained.

Diagnostics obtained from the numerical solutions were the shock trajectory and the gas conditions immediately behind the shock. The shock position R_s was found as an average of the front and back of the shock profile. The front of the shock was located at the first deviation of density and radial velocity from pre-shock conditions; the back of the shock was calculated as the local maximum in the squared perturbation magnetic field $(B_\theta^1)^2$. Post-shock values of pressure and density were calculated from a point immediately behind the back of the shock. The corresponding pressure and density ratios across the shock were then used in the shock jump condition, (15)–(17) to calculate the shock Mach number. For the line-current case, the value $r = R_s$ was used in the second equation of Eqs. (43) where $\epsilon(r)$ appears in the shock-jump conditions. The upstream magnetic field used for this case was calculated using the radius defining the front of the shock.

The convergence of numerical solutions for shock quantities was explored using exponentially stretch grids with $N = 4 \times 10^3$, 8×10^3, 16×10^3 for the case with $M_0 = 2.0$, $r_0 = 10^2$. Plots of $M(r)$ for these grids showed differences of order the line thickness and so are not displayed. Instead we discuss convergence of the maximum Mach number M_{max} achieved. For $N = 4 \times 10^3$, 8×10^3, 16×10^3 we obtained $M_{max} = 23.564, 23.795, 23.871$, respectively. Richardson extrapolation based on these values with variable order of convergence gives $M_{max} = 23.958$ with order of convergence 0.90. This is consistent with the use of a shock-capturing method. The relative error on the finest grid from Richardson extrapolation is 0.00446.
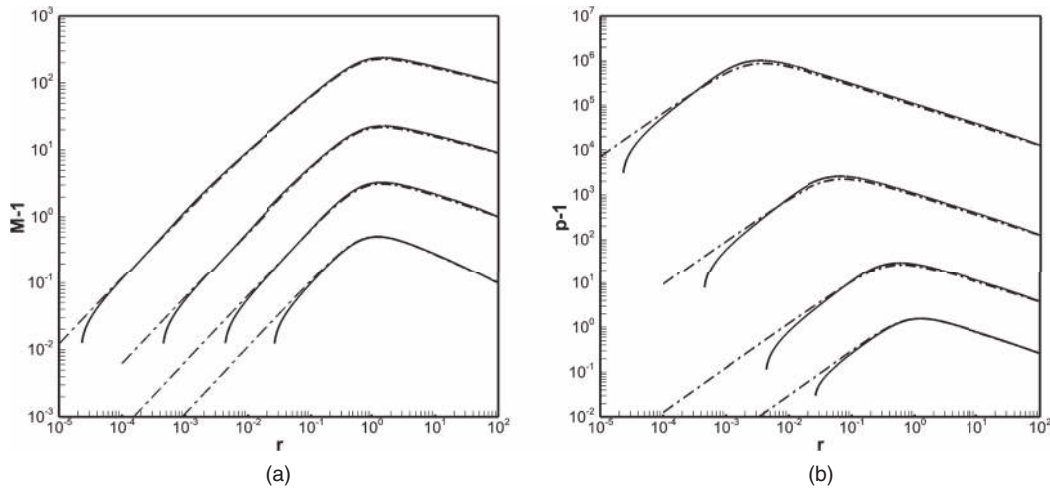
FIG. 5. Comparison of shock-dynamics and numerical solutions. (a) $M(r) - 1$ and (b) $p(r) - 1$. Solid lines: numerical; dashed-dotted: shock dynamics. From top to bottom: M_0 at $r_0 = 10^2$ with $M_0 = 100, 10, 2, 1.1$.

Figures 5 and 6 show comparison between the numerical and the shock-dynamics solutions and also illustrate the range in radius achieved by the latter. In Figure 5(a), depicting $M - 1$ versus r, the differences between the shock-dynamics and numerical solutions are generally of order a few percent across almost the whole radial range of the latter except over the final half-decade where the numerical solutions uniformly dip below the shock-dynamics predictions. This behavior occurs because of a smearing of a shock profile for low r; this shock smearing causes the local maximum in the perturbed field itself to smear, so that the various detected post-shock values may no longer be representative of the true post-shock conditions. For further decreasing r, the local field maximum becomes indistinct and eventually disappears, leading to failure of the detection method. Shock-dynamics correctly calculates the qualitative variation of pressure jump with radius in Figure 5(b) including the inward movement of the maximum pressure jump with increasing initial M_0.

We quantify the differences between numerical and GSD results by considering both the pressure and Mach number at their respective maxima for all cases. Table II shows these scaled against p_{max} and M_{max} obtained from the numerical solutions. The relative discrepancies $\Delta p/p_{max}$ and $\Delta M/M_{max}$ are small for $M_0 = 1.1$ but the differences increase as M_0 increases.
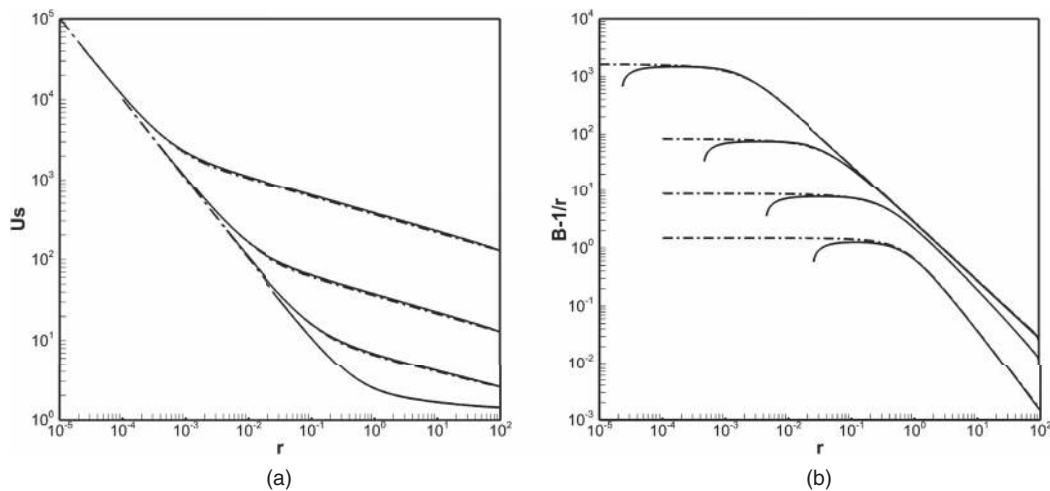

FIG. 6. Comparison of shock-dynamics and numerical solutions. (a) Shock speed and (b) perturbation magnetic field behind shock. Solid lines: numerical; dashed-dotted: shock dynamics. For key, see Figure 5.

TABLE II. Relative pressure and Mach number discrepancies between numerical and shock-dynamics solutions for four cases, each at its maximum value.

M_0	$\frac{\Delta p}{p_{max}}$	$\frac{\Delta M}{M_{max}}$
1.1	0.00548	0.00534
2.0	0.0948	0.0348
10.0	0.135	0.0438
100.0	0.140	0.0439

For both the shock-dynamics and the numerical solutions, the shock speed U_s in Figure 6(a) is seen to accelerate with decreasing radius. For the three cases with $M_0 = 100, 10, 2$, the imploding shock at first follows closely the strong shock collapse profile while for $M_0 = 1.1$ the maximum Mach number achieved is $M \sim 1.5$ and so a strong-shock phase is not achieved. For sufficiently small radius, all profiles show asymptotic approach to the MHD sonic speed $c_0 \sim r^{-1}$.

The tangential magnetic-field strength behind the shock is given by (18). Figure 6(b) shows the perturbation magnetic field behind the shock, $B_\theta^1 = B_\theta - B_\theta^0$ with $B_\theta^0 = 1/r$. Equation (18) shows that $B_\theta^1 = (\rho/\rho_0 - 1)/r$, and using Eq. (20) then gives that

$$B_\theta^1 = \frac{1}{r} \frac{4}{3} (M - 1) + \ldots . \tag{59}$$

Using (47) then gives $B_\theta^1 \to 4A/3$ when $r \to 0$, hence becoming asymptotically constant at a strength that depends on the initial conditions. In Figure 6(b) both the numerical and shock-dynamics calculations appear to confirm this although the regions over which this asymptotic state is reached using the former decrease for decreasing M_0. A similar calculation using the first equation of (18) gives that the gas velocity immediately behind the shock in the laboratory frame of reference approaches the finite value $u \to -4A/3$ when $r \to 0$. These results are consistent with (12).

Figure 7 illustrates $u - c$ characteristics obtained by integration of the equation $dr/dt = u - c$ using a range of initial conditions and with (u, c) obtained from the numerical solutions. The two cases shown are $M_0 = 10, r_0 = 100$ and $M_0 = 100, r_0 = 100$. In both images, (negative) time increases top to bottom and the shock trajectory towards the axis is shown by the black line. The undisturbed region is to the upper left in both plots. The region to the lower-right lies behind the shock. The characteristics that intersect the shock in this region are the families that form the basis of the shock-dynamics approximation. In the images, the characteristic curves are distorted by use of $\log(r) - \log(-t)$ co-ordinates. Those to the extreme right of the shock will pass through $t = 0$ with finite r and will eventually intersect a reflected shock, which is not considered presently. There
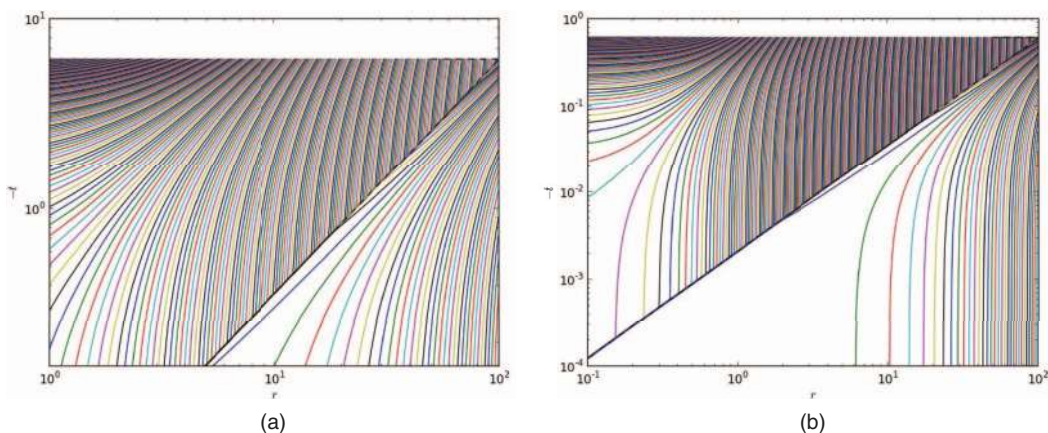

FIG. 7. $u - c$ characteristics in $(-t, r)$ plane for two different M_0, $r_0 = 100$.

exists a last characteristic which will become tangent to the shock with $dr/dt \to 0$ when $t \to 0$. For the case $M_0 = 100$ in Figure 7(b), this can be expected to lie somewhere between the $u - c$ characteristic that can be seen intersecting the shock and the first characteristic to the lower right that, in the plot, appears as almost vertical. This last characteristic is difficult to capture from the numerical solutions.

We now comment on breakdown of the ideal MHD approximation. First, the shock thickness scales with the mean free path; thus when the shock radius is of the order of the mean free path, the shock thickness cannot be neglected and our assumptions breakdown. This also applies to the hydrodynamic case.[27] Second, for the hydrodynamic and magnetic Reynolds numbers we use density, velocity, and length scales as those immediately downstream of the shock, ρ and u, and the shock radius R_s, respectively. Both Reynolds numbers are proportional to the product of these three scales. In all cases considered, ρ approaches a constant value as the shock converges, as does u for the line current case. In the axial field case, u increases like $R_s^{-1/n}$ in the strong shock limit where from (31), $1 - 1/n > 0$. Thus for both fields, the Reynolds numbers decrease with shock radius near convergence. For any finite viscosity and resistivity, this implies that for sufficiently small shock radii the Reynolds number will no longer be large, and hence viscous and resistive effects will become important. Another potential cause for breakdown of the ideal MHD approximation is the shock radius approaching the ion Larmor radius, which scales linearly with the velocity normal to the magnetic field and inversely with B. In the axial field case, u grows large near convergence while B asymptotes to a constant value. Thus the Larmor radius is speculated to increase, causing ideal MHD to breakdown as $R_s \to 0$. In the line current case, the increase in B balances the decrease in r as the shock converges, while u asymptotes to a constant value. In this case, we speculate that the Larmor radius does not approach the shock radius near convergence.

VI. CONCLUDING REMARKS

Presently we have investigated the implosion of a cylindrical shock wave within the framework of ideal magnetohydrodynamics, for field configurations in which the magnetic field lines are perpendicular to radially inwards particle paths behind the shock. Two approaches were explored. The first is Whitham's geometrical shock dynamics obtained by substituting the restricted shock-jump conditions, obtained as a function of both shock Mach number and a parameter representing the magnetic field strength ahead of the shock, into the state variables contained in the equation on the characteristic entering the shock from behind. This leads to an ordinary differential equation for the shock Mach number as a function of radius. This equation is cumbersome but does yield leading-order asymptotic results for both large shock Mach number and for Mach number of order unity. It can also be readily solved numerically. The second approach is the numerical solution, using a shock-capturing method, of the one-dimensional ideal magnetohydrodynamic equation on a radially stretched grid.

Two distinct magnetic field configurations were investigated: an axial field of constant strength and an azimuthal field generated by a line current along the axis of shock convergence. For the former, a large Mach number analysis of the shock-dynamics equation indicates that the presence of a transverse axial field does not change the convergence as described by the Guderley[3,20] algebraic, strong-shock intensification as $M \sim r^{-1/n(\gamma)}$ where $n(\gamma)$ is the same as for the strong-shock, pure gas-dynamics case. Numerical solutions, not shown presently, confirm this behavior. Although not proven presently, we expect this result to be typical of a more general axial field variation $B_z(r)$ provided that $B_z(r = 0)$ is finite.

When the magnetic field is azimuthal with variation inversely proportional to radius as generated by a line current, then both the shock dynamics and the numerical solutions show a very different shock collapse scenario. A one-parameter family of shock collapse profiles exists characterized by a specified supersonic Mach number at any fixed shock radius. Further, there exists a critical radius R determined by the line-current strength and the ambient pressure and plasma permeability, at which the normalized magnetic field is order one. For initial shock radius larger than R, there ensues a competition between shock intensification owing to geometrical convergence and increasing magnetic field strength. Initially convergence is dominant in the presence of a weak magnetic

field where an epoch of strong shock gas-dynamic convergence can be seen. As the shock radius decreases below R, the increasing magnetic field strength leads to a dominant Lorentz force and a rapidly increasing fast magnetosonic speed ahead of the shock. This effect overpowers geometrical convergence with the result that the shock Mach number reaches a maximum followed by decreasing linearly with shock radius towards a limiting magnetosonic state. The shock speed, however continues to accelerate approaching the increasing magnetosonic speed. Past the critical radius, the shock pressure jump may continue to increase reaching a large maximum at a radius smaller than R that depends on the initial shock strength, followed by subsequent decrease. In fact for initially strong shocks, very large pressure and therefore temperature ratios can be achieved across shocks whose Mach number differs by order 1% from unity.

As discussed in Sec. I, interest in the present shock convergence properties is motivated by the application of seed magnetic fields in ICF experiments. The proposed application of a magnetic field generated by a seed current through an axial thin wire to further enhance electron confinement in ICF experiments[18] is similar to the present line-current case. Our results indicate that this magnetic field has the potential to weaken the shock when it is close to convergence, limiting the temperature and pressure achieved at the center of the implosion. Somewhat surprisingly, even though shock strength eventually decays for the line-current case, strong pressure jump conditions can still be achieved at quite small shock radius. Thus there is the potential to mitigate this effect through a careful choice of experimental parameters.

ACKNOWLEDGMENTS

[1] J. D. Lindl, R. L. McCrory, and E. M. Campbell, "Progress toward ignition and burn propagation in inertial confinement fusion," Phys. Today **45**(9), 32 (1992).

[2] R. Betti, P. Y. Chang, B. K. Spears, K. S. Anderson, J. Edwards, M. Fatenejad, J. D. Lindl, R. L. McCrory, R. Nora, and D. Shvarts, "Thermonuclear ignition in inertial confinement fusion and comparison with magnetic confinementa)," Phys. Plasmas **17**(5), 058102 (2010).

[3] G. Guderley, "Starke kugelige und zylindrische Verdichtungsstösse in der Nähe des Kugelmittelpunktes bzw. der Zylinderachse," Luftfahrtforschung **19**, 302–312 (1942).

[4] D. S. Butler, "Converging spherical and cylindrical shocks," Armament Res. Estab. Rep. **54**, 54 (1954).

[5] R. F. Chisnell, "The motion of a shock wave in a channel, with applications to cylindrical and spherical shock waves," J. Fluid Mech. **2**(03), 286–298 (1957).

[6] G. B. Whitham, "A new approach to problems of shock dynamics. Part 1. Two-dimensional problems," J. Fluid Mech. **2**(02), 145–171 (1957).

[7] G. B. Whitham, "A new approach to problems of shock dynamics. Part 2. three-dimensional problems," J. Fluid Mech. **5**(03), 369–386 (1959).

[8] G. B. Whitham, *Linear and Nonlinear Waves* (John Wiley & Sons, 2011).

[9] J. E. Cates and B. Sturtevant, "Shock wave focusing using geometrical shock dynamics," Phys. Fluids (1994-present) **9**(10), 3058–3068 (1997).

[10] W. D. Henshaw, N. F. Smyth, and D. W. Schwendeman, "Numerical shock propagation using geometrical shock dynamics," J. Fluid Mech. **171**, 519–545 (1986).

[11] C. J. Catherasoo and B. Sturtevant, "Shock dynamics in non-uniform media," J. Fluid Mech. **127**, 539–561 (1983).

[12] N. F. Ponchaut, H. G. Hornung, D. I. Pullin, and C. A. Mouton, "On imploding cylindrical and spherical shock waves in a perfect gas," J. Fluid Mech. **560**, 103–122 (2006).

[13] H. G. Hornung, D. I. Pullin, and N. F. Ponchaut, "On the question of universality of imploding shock waves," Acta Mech. **201**(1–4), 31–35 (2008).

[14] R. D. Richtmyer, "Taylor instability in shock acceleration of compressible fluids," Commun. Pure Appl. Math. **13**(2), 297–319 (1960).

[15] E. E. Meshkov, "Instability of the interface of two gases accelerated by a shock wave," Fluid Dyn. **4**(5), 101–104 (1969).

[16] R. Samtaney, "Suppression of the Richtmyer–Meshkov instability in the presence of a magnetic field," Phys. Fluids (1994-present) **15**(8), L53–L56 (2003).

[17] V. Wheatley, R. Samtaney, and D. I. Pullin, "The Richtmyer–Meshkov instability in magnetohydrodynamics," Phys. Fluids (1994-present) **21**(8), 082102 (2009).

[18] H. Hohenberger, P. Y. Chang, G. Fiskel, J. P. Knauer, R. Betti, F. J. Marshall, D. D. Meyerhofer, F. H. Séguin, and R. D. Petrasso, "Inertial confinement fusion implosions with imposed magnetic field compression using the OMEGA Laser," Phys. Plasmas **19**, 056306 (2012).

[19] G. B. Whitham, "On the propagation of shock waves through regions of non-uniform area or flow," J. Fluid Mech. **4**(04), 337–360 (1958).

[20] R. M. Gundersen, "The propagation of non-uniform magnetohydrodynamic shocks, with special reference to cylindrical and spherical shock waves," Arch. Ration. Mech. Anal. **11**(1), 1–15 (1962).

[21] M. A. Liberman and A. L. Velikovich, "Self-similar motions in z-pinch dynamics," Nucl. Fusion **26**(6), 709 (1986).

[22] A. L. Velikovich, J. L. Giuliani, S. T. Zalesak, J. W. Thornhill, and T. A. Gardiner, "Exact self-similar solutions for the magnetized Noh z pinch problem," Phys. Plasmas (1994-present) **19**(1), 012707 (2012).

[23] R. Samtaney, P. Colella, T. J. Ligocki, D. F. Martin, and S. C. Jardin, "An adaptive mesh semi-implicit conservative unsplit method for resistive MHD," J. Phys.: Conf. Ser. **16**, 40 (2005).

[24] K. G. Powell, P. L. Roe, T. J. Linde, T. I. Gombosi, and D. L. De Zeeuw, "A solution-adaptive upwind scheme for ideal magnetohydrodynamics," J. Comput. Phys. **154**(2), 284–309 (1999).

[25] V. Wheatley, D. I. Pullin, and R. Samtaney, "Regular shock refraction at an oblique planar density interface in magnetohydrodynamics," J. Fluid Mech. **522**, 179–214 (2005).

[26] V. Wheatley, R. Samtaney, D. I. Pullin, and R. M. Gehre, "The transverse field Richtmyer-Meshkov instability in magnetohydrodynamics," Phys. Fluids **26**(1), 016102 (2014).

[27] M. J. Goldsworthy and D. I. Pullin, "Mean free path effects in the shock-implosion problem," Phys. Fluids (1994-present) **21**(2), 026101 (2009).